https://doi.org/10.5194/egusphere-2026-4160
Preprint. Discussion started: 24 July 2026

Intense concentric gravity waves from the stratosphere to the thermosphere and a massive red sprite outbreak triggered by severe thunderstorms South of the Himalayas

Qinzeng Li[1], Jiyao Xu[1], Wei Yuan[1], Angel An[2], Shengyang Gu[3], Oscar A. van der Velde[4], Yajun Zhu[1,5], and Xiaolong Wei[1,6]

1. State Key Laboratory of Solar Activity and Space Weather, National Space Science Center, Chinese Academy of Sciences, Beijing, 100190, China
2. Independent photographer: Beijing, 100000, China
3. School of Earth and Space Science and Technology, Wuhan University, Wuhan, China
4. Department of Electrical Engineering, Universitat Politécnica de Catalunya, Colom 1, 08222 Terrassa, Spain
5. National Field Observation and Research Station (Hainan) for Space Weather, Hainan, China
6. College of Earth and Planetary Sciences, University of Chinese Academy of Sciences, Beijing, 100049, China

Correspondence: Jiyao Xu (jyxu@swl.ac.cn)

https://doi.org/10.5194/egusphere-2026-4160
Preprint. Discussion started: 24 July 2026

Abstract

Severe thunderstorms drive vertical coupling through electrical processes associated with transient luminous events (TLEs) and dynamical processes associated with atmospheric gravity waves (AGWs). On 19 May 2022, an exceptionally intense thunderstorm outbreak occurred over the northern Bay of Bengal–Himalayan foothill region. The storm system produced more than 100 red sprites, 16 secondary gigantic jets, and at least four ghosts, accompanied by visible concentric airglow ripples. This event represented the first large-scale detection of a massive red sprite outbreak in China. From a dynamical perspective, concentric gravity waves (CGWs) were observed from the stratosphere to the thermosphere using coordinated satellite and ground-based airglow observations. AIRS measurements revealed concentric wave structures in the stratosphere above the convective source region, while ground-based airglow imagers detected CGWs in the OH, OI 557.7 nm, and OI 630.0 nm emission layers. CGWs in the mesosphere and lower thermosphere (MLT) propagated northeastward for more than 3000 km, suggesting propagation within favorable MLT ducting structures. In contrast, thermospheric CGWs observed in the OI 630.0 nm emission exhibited horizontal phase speeds of 260–280 m s^{-1}. Reverse ray-tracing analysis indicates a preferred source altitude near 150 km, suggesting that these waves were likely secondary gravity waves generated by the dissipation and breaking of upward-propagating primary gravity waves. Their asymmetric occurrence is likely attributable to Doppler-induced dissipation associated with thermospheric background winds. These observations provide a rare example of simultaneous electrical and dynamical

https://doi.org/10.5194/egusphere-2026-4160
Preprint. Discussion started: 24 July 2026

coupling from the troposphere to the thermosphere during an extreme convective event.

https://doi.org/10.5194/egusphere-2026-4160
Preprint. Discussion started: 24 July 2026

1. Introduction

Severe thunderstorms influence the upper atmosphere through both dynamical and electrical pathways. Dynamically, latent heat release and overshooting convective motions generate atmospheric gravity waves (AGWs) that can propagate from the troposphere into the mesosphere and thermosphere (Fovell et al., 1992; Alexander and Holton, 2004; Heale et al., 2019, 2022; Smith et al., 2020; Nyassor et al., 2022; Li et al., 2025). As AGWs propagate upward through the decreasing-density atmosphere, their amplitudes increase and may eventually become convectively or dynamically unstable. Subsequent wave breaking deposits momentum and energy into the background atmosphere and can generate secondary gravity waves that continue propagating into higher atmospheric regions (Holton, 1983; Vadas et al., 2003; Smith et al., 2013; Li et al., 2022). Through these processes, AGWs transfer energy and momentum across atmospheric layers and constitute one of the primary mechanisms responsible for vertical atmospheric coupling (Fritts and Alexander, 2003; Plane et al., 2023).

Electrically, intense thunderstorms can produce transient luminous events (TLEs), including red sprites, gigantic jets, and other high-altitude optical emissions above active storm systems (Pasko et al., 1997; Sentman et al., 2003; Chou et al., 2016; Wang et al., 2019; Lai et al., 2022; Maurya et al., 2022). Red sprites are among the most common TLEs and typically occur in the mesosphere above powerful positive cloud-to-ground lightning discharges. Particularly intense sprite outbreaks may also be accompanied by rare phenomena such as secondary gigantic jets and ghosts (van der

https://doi.org/10.5194/egusphere-2026-4160
Preprint. Discussion started: 24 July 2026

Velde et al., 2019; Passas-Varo et al., 2023). Although both TLEs and AGWs originate from the same convective source, observations simultaneously revealing the electrical and dynamical impacts of extreme thunderstorms across multiple atmospheric layers remain relatively rare.

The northern Bay of Bengal–Himalayan foothill region is a major hotspot of deep convection and atmospheric disturbances in the Earth system (Maurya et al., 2022; Peng et al., 2024). On the night of 19 May 2022, an exceptionally intense thunderstorm outbreak occurred over the northern Bay of Bengal–Himalayan foothill region. The storm system produced more than 100 red sprites, 16 secondary gigantic jets, and four ghosts, representing the largest documented sprite outbreak observed from China. Simultaneously, distinct concentric airglow ripples were recorded, suggesting strong gravity-wave activity associated with the convective system. Subsequent observations revealed concentric gravity waves (CGWs) spanning from the stratosphere to the thermosphere, providing a unique opportunity to investigate both the electrical and dynamical impacts of an extreme convective event on the middle and upper atmosphere.

In this study, we use coordinated observations from ground-based airglow imagers, AIRS stratospheric measurements, TIMED/SABER observations, and Meteosat/SEVIRI imagery to investigate the CGWs associated with this exceptional thunderstorm outbreak. Particular attention is given to (1) the long-distance propagation of CGWs in the mesosphere and lower thermosphere (MLT), (2) the generation mechanism of thermospheric CGWs, and (3) the role of thermospheric background winds in modulating CGW observability. The observations provide a rare example of

https://doi.org/10.5194/egusphere-2026-4160
Preprint. Discussion started: 24 July 2026

deep-convection-driven vertical coupling extending from the troposphere to the thermosphere and reveal distinct propagation characteristics of mesospheric and thermospheric CGWs.

2. Observations

2.1 Ground-based airglow observations and amateur photography imaging

Figure 1 presents the location map of airglow observation stations at Lhasa (30.1°N, 90.6°E), Xining (36.5°N, 102.1°E), Shuozhou (39.8°N, 112.1°E), Xinglong (40.2°N, 117.4°E), and Korla (41.7°N, 86.2°E). The airglow observation station in Lhasa is equipped with three dedicated airglow imagers for multi-layer monitoring. The three imagers observe distinct emission layers: one observes the hydroxyl (OH) airglow near 87 km altitude with a 63-second temporal resolution; a second is configured for atomic oxygen emission at 557.7 nm (OI 557.7 nm) originating from approximately 96 km; and a third detects the OI 630.0 nm emission near 250 km altitude. The two oxygen emission imagers (OI 557.7 nm and OI 630.0 nm) both operate with a 92-second temporal resolution. This coordinated instrument array enables simultaneous observations of mesospheric (OH and OI 557.7 nm) and thermospheric (OI 630.0 nm) airglow emissions. The Xining, Shuozhou, Xinglong, and Korla stations are equipped with OH and OI 630.0 nm imagers identical to those deployed at Lhasa, but do not include the OI 557.7 nm channel. In addition to the scientific airglow imaging instruments, supplementary time-lapse photographs of the sprite event were obtained using three Sony Alpha 7RIII cameras equipped with 14 mm, 35 mm, and 135 mm lenses, respectively, with 5 s exposures at f/1.4.

https://doi.org/10.5194/egusphere-2026-4160
Preprint. Discussion started: 24 July 2026

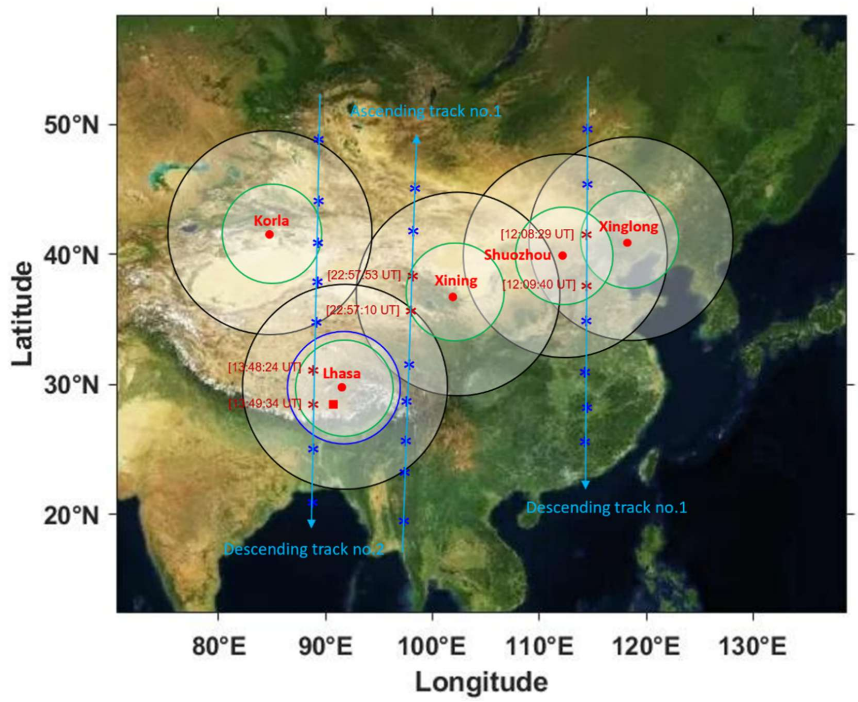

Figure 1 Map showing the geographic location of the airglow imagers station in Lhasa, Xining, Shuozhou, Xinglong, and Korla (red dots) and red-sprite observation site documented by amateur photographers (red square). The circle on the map gives the effective observation ranges of OH airglow imagers and red-line (630 nm) imagers with a 164° field of view. The red asterisks denote the TIMED/SABER descending track footprints passing over Lhasa on 19 May 2022.

2.2 Aqua/AIRS satellite observations

Mounted on NASA's Aqua satellite, the AIRS (Aumann et al., 2003) employs infrared spectroscopy for atmospheric sounding. The instrument conducts continuous scans perpendicular to the satellite track, sequentially sampling atmospheric radiance within footprints measuring approximately 13–14 km across at nadir. This scanning pattern yields a swath width of ~1765 km (Hoffmann et al., 2014), with data typically aggregated into 6-minute granules. AIRS exhibits sensitivity to atmospheric temperature fluctuations induced by GWs, specifically detecting perturbations

https://doi.org/10.5194/egusphere-2026-4160
Preprint. Discussion started: 24 July 2026

associated with vertical wavelengths exceeding 10–15 km and horizontal wavelengths between ~50 and500 km (Hoffmann and Alexander, 2010). In this study, radiance measurements within the 4.3 μm CO_2 fundamental band are employed. This spectral region is highly sensitive to temperature perturbations in the stratosphere, particularly between altitudes of 30–40 km, making it well suited for quantifying stratospheric temperature perturbations.

2.3 TIMED/SABER satellite observations

Aboard NASA's TIMED satellite (launched Dec. 7, 2001), SABER is a 10-channel broadband limb-scanning infrared radiometer (1.27–17 μm) (Russell et al., 1999) that provides key observations for investigating energy transfer processes in the Mesosphere–Lower Thermosphere–Ionosphere (MLTI) region. SABER measures kinetic temperature (±2–5 K) using CO_2 emissions, including the 15 μm LTE channel below ~90 km and the 4.3 μm non-LTE channel at higher altitudes. By simultaneously observing emissions from O_3 (9.6 μm), OH (1.6–2.0 μm), and O_2 (1.27 μm), SABER quantifies key thermal processes, including radiative cooling (reaching 150 K day^{-1}) and chemical heating (~8 K day^{-1}). These measurements, with a 2–4 km vertical resolution, characterize the thermal structure and background state of the MLT region.

2.4 Meteosat/SEVIRI satellite observations

The Meteosat series, operated by EUMETSAT, is Europe's primary geostationary meteorological satellite system, providing continuous observations of atmospheric and convective processes over Europe, Africa, and adjacent regions. The primary instrument aboard the Meteosat Second Generation (MSG) satellites (Schmetz et al.,

https://doi.org/10.5194/egusphere-2026-4160
Preprint. Discussion started: 24 July 2026

2002) is SEVIRI, which acquires full-disk images every 15 minutes across 12 spectral bands.

2.5 SD-WACCM-X and TIE-GCM 3.0 simulations

SD-WACCM-X (the Specified Dynamics Whole Atmosphere Community Climate Model with thermosphere-ionosphere eXtension) is a whole atmosphere model developed within the NCAR Community Earth System Model (CESM) framework (Hurrell et al., 2013; Liu et al., 2018). Its domain extends from the Earth's surface to the upper thermosphere. The specified dynamics configuration enables improved representation of upward-propagating atmospheric waves. TIE-GCM 3.0 (the Thermosphere–Ionosphere–Electrodynamics General Circulation Model, Version 3.0) is a first-principles numerical model that self-consistently simulates the coupled thermosphere-ionosphere system in the upper atmosphere (approximately 97–600 km altitude) (Richmond et al., 1992; Günzkofer et al., 2025). The model includes self-consistent electrodynamics and ion-neutral coupling processes that are important for thermosphere-ionosphere dynamics.

3. Results and Discussion

The extreme convective event produced both electrical and dynamical responses in the middle and upper atmosphere. The electrical response was manifested by an exceptional TLE outbreak, including red sprites, secondary gigantic jets, and ghosts, reflecting intense lightning activity extending into the middle atmosphere. The dynamical response involved the generation, propagation, and secondary excitation of gravity waves from the stratosphere to the thermosphere.

https://doi.org/10.5194/egusphere-2026-4160
Preprint. Discussion started: 24 July 2026

3.1 Convective evolution and transient luminous event outbreak

Figure 2 shows continuous SEVIRI 10.8 μm brightness temperature imagery from the Meteosat Second Generation (MSG) satellite during 10:00–21:00 UT on 19 May 2022. The imagery reveals the evolution of a deep convective system located along the southern foothills of the Himalayas. At 10:00 UT, the system initially appeared as multiple isolated convective cells with cold cloud tops distributed over approximately 23–27°N and 85–93°E. Between 11:00 and 12:00 UT, these individual cells rapidly intensified and merged, forming a more organized mesoscale convective system (MCS) with substantial eastward expansion. This period was characterized by vigorous deep convection and enhanced latent heat release, conditions favorable for the excitation of atmospheric GWs. The convective system also served as the parent storm of the subsequent transient luminous event outbreak.

Between 13:00 and 15:00 UT, the MCS reached its mature stage, characterized by a large and consolidated cold cloud shield extending across approximately 22–28°N and 85–90°E. Persistently low brightness temperatures indicate strong vertical convective development penetrating into the upper troposphere and lower stratosphere. From 16:00 to 18:00 UT, the convective system gradually weakened and fragmented, accompanied by contraction of the cold cloud shield. By 19:00–21:00 UT, only scattered remnants of stratiform cloud structures remained over 22–28°N and 88–94°E, indicating the dissipation of the previously organized convective system. This exceptionally intense convective system subsequently produced one of the largest transient luminous event outbreaks observed from China.

https://doi.org/10.5194/egusphere-2026-4160
Preprint. Discussion started: 24 July 2026

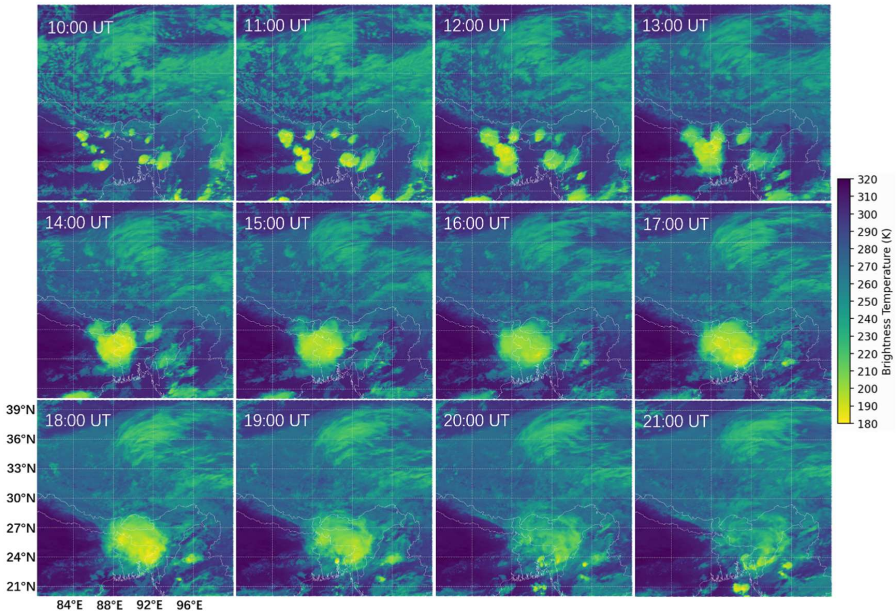

Figure 2 SEVIRI 10.8 μm channel brightness temperature composite from Meteosat Second Generation (MSG) during 10:00–21:00 UT on 19 May 2022.

Figure 3 presents representative images of the TLE outbreak associated with the convective system shown in Fig. 2. The images were captured using time-lapse photography by photography enthusiasts from the shores of Lake Pumoyongcuo in Shannan, Tibet, on the night of 19 May 2022. The outbreak persisted for approximately three hours, from 13:00 to 16:00 UT, coinciding with the mature stage of the parent mesoscale convective system. More than 100 red sprites, 16 secondary gigantic jets, and four ghosts were recorded during this period, making it the largest documented sprite outbreak observed from China (Huang et al., 2025). The images shown in Fig. 3 represent only a subset of the observed activity. Various sprite morphologies, including carrot-shaped and columniform structures, were observed, often occurring in large clusters over a broad horizontal region above the parent storm. Particularly notable are

https://doi.org/10.5194/egusphere-2026-4160
Preprint. Discussion started: 24 July 2026

the secondary gigantic jets visible at 13:16 UT and the extensive sprite clusters observed around 13:19–13:42 UT. The simultaneous occurrence of numerous sprites together with multiple secondary gigantic jets and ghosts indicates exceptionally intense electrical activity within the parent convective system.

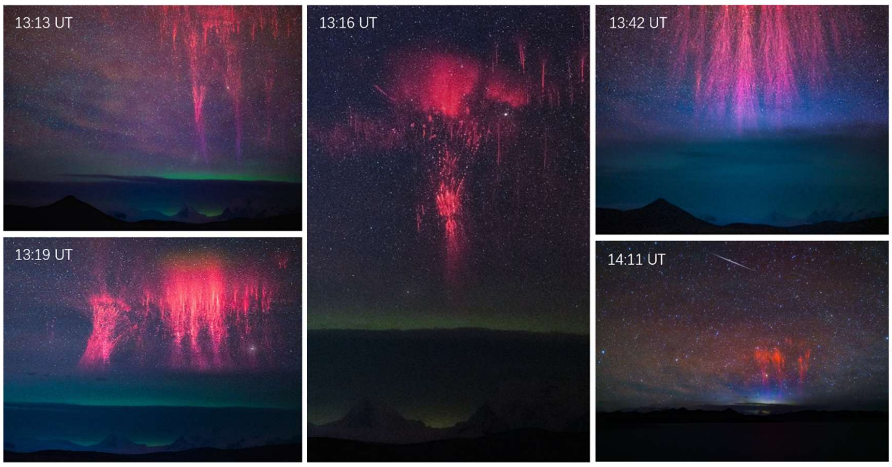

Figure 3 Transient luminous events (TLEs) captured by amateur photographer Angel An over the southern Tibetan Plateau on the night of 19 May 2022, showcasing a variety of red sprite morphologies. Photographs © Angel An.

3.2 Stratospheric concentric gravity waves from the AIRS/Aqua

Figure 4 shows annular GWs in AIRS 4.3 μm brightness temperature perturbations (19:23:21 UT, 19 May 2022), exhibiting concentric wave fronts centered over northeastern Bangladesh (~25°N, 88°E). These waves display a distinct radial wavelength gradient, with horizontal wavelengths increasing from ~50 km near the central region to >150 km at the periphery. The observed concentric structures are spatially associated with the previously identified deep convective system and suggest active wave excitation in the stratosphere during the late stage of convective evolution.

https://doi.org/10.5194/egusphere-2026-4160
Preprint. Discussion started: 24 July 2026

Although the primary convective cloud shield had weakened by this time, localized convective activity may still have contributed to the generation of the observed CGWs.

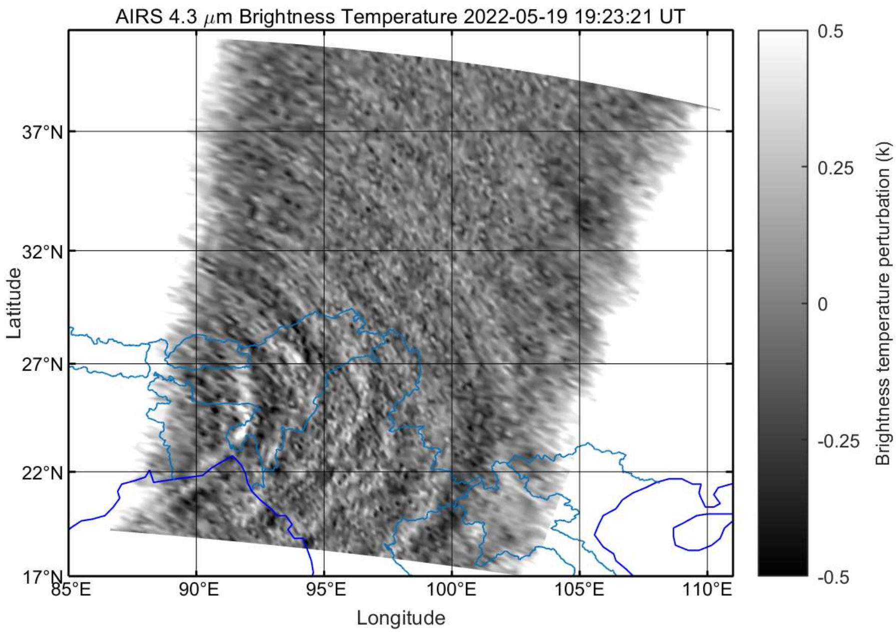

Figure 4 CGWs observed by Aqua/ARIS at 4.3 μm brightness temperature on 19 May 2022 at 19:23:21 UT.

3.3 Multi-layers ground-based optical observations of concentric gravity waves from the mesosphere to the thermosphere

Figure 5 presents a sequence of time-lapse photographs acquired from the shores of Lake Pumoyongcuo between 15:19 and 15:43 UT on 19 May 2022. In addition to the transient luminous events, a series of faint concentric airglow ripples can be identified across the night sky. These ripples appeared as multiple arc-shaped bands extending over a broad horizontal region and exhibited a clear concentric geometry, suggesting the presence of concentric gravity waves (CGWs) propagating through the mesopause airglow layer. The wave fronts remained visible for more than 20 min and

https://doi.org/10.5194/egusphere-2026-4160
Preprint. Discussion started: 24 July 2026

gradually expanded across the field of view. Simultaneously, sprite activity continued above the distant convective system, indicating that both the electrical phenomena and the airglow disturbances were associated with the same parent thunderstorm. Although the photographic observations do not permit quantitative determination of wave parameters, they provide direct visual evidence of large-scale concentric wave structures accompanying the exceptional convective outbreak.

https://doi.org/10.5194/egusphere-2026-4160
Preprint. Discussion started: 24 July 2026

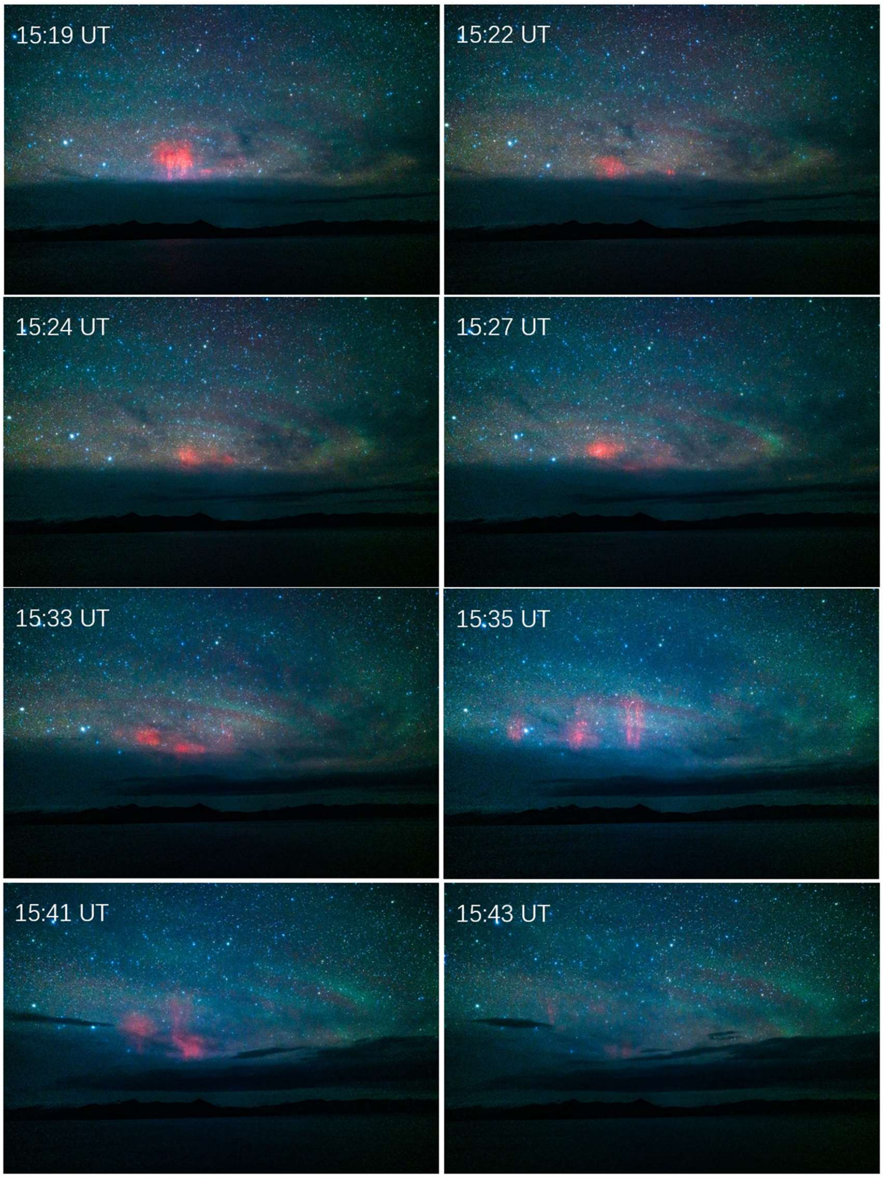

Figure 5. Temporal sequence of concentric gravity waves (CGWs) observed during the red sprite outbreak over the southern Tibetan Plateau from 15:19 to 15:43 UT on 19 May 2022. Photographs © Angel An.

Figure 6 presents multi-layer airglow observations at the Lhasa station, revealing concentric gravity wave structures observed in the mesosphere, mesopause region, and

https://doi.org/10.5194/egusphere-2026-4160
Preprint. Discussion started: 24 July 2026

thermosphere. Figure 6a shows OI (630.0 nm) airglow observations at ~250 km altitude, where large-scale concentric wave fronts are visible in the thermospheric F-region. Figure 6b displays OI (557.7 nm) airglow observations near ~96 km, showing multiple concentric gravity wave packets in the mesopause region. Figure 6c depicts OH airglow observations at ~87 km, revealing pronounced concentric wave structures in the MLT region.

The wave morphology and propagation characteristics exhibit notable differences among the three emission layers. The OH and OI (557.7 nm) emissions display clearer and more coherent concentric wave fronts in the MLT region, whereas the OI (630.0 nm) emission exhibits broader and more diffuse thermospheric wave structures. Despite these differences, the observed wave patterns are spatially associated with the same deep convective system to the south of the Himalayas. The simultaneous detection of concentric gravity wave signatures over a broad altitude range suggests strong vertical coupling between the lower atmosphere and the upper atmosphere during this event.

https://doi.org/10.5194/egusphere-2026-4160
Preprint. Discussion started: 24 July 2026

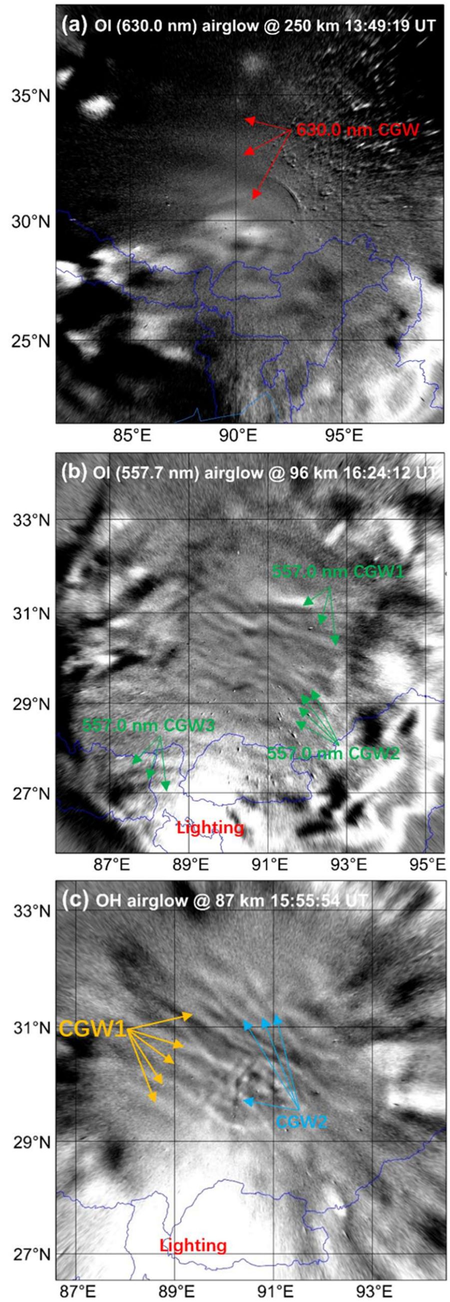

255

256 **Figure 6** Multi-layer airglow observations of CGWs at Lhasa station, showing emissions from three
257 different altitudes: (a) OI 630.0 nm (thermospheric airglow, ~250 km); (b) OI 557.7 nm
258 (mesospheric airglow, ~97 km); (c) OH band (mesospheric airglow, ~87 km).

https://doi.org/10.5194/egusphere-2026-4160
Preprint. Discussion started: 24 July 2026

To estimate the wave parameters of the CGWs shown in Fig. 5 captured by astrophotography enthusiasts, we used a star chart to precisely determine the elevation (el) and azimuth angle (az) of the stars in the image. The horizontal distances between the observation point and the airglow layer can be calculated using the following equation (Yue and Lyons, 2015):

$$s = R*\left[\pi/2 - el - \sin^{-1}\left(\frac{R*\sin(el+\pi/2)}{R+H}\right)\right], \qquad (1)$$

where R is the Earth's radius, and H is the altitude of the airglow layer.

The horizontal coordinates (x, y) within the airglow layer can then be expressed as follows,

$$x = s*\sin(az), \qquad (2)$$

$$y = s*\cos(az), \qquad (3)$$

The horizontal wavelength of the concentric wave structures was estimated to be approximately 38 ± 5 km. This value is consistent with the horizontal wavelength of CGW1 observed at 15:55:54 UT in Fig. 6c, suggesting that the ripple structures captured by the amateur photographer and the CGW observed by the ground-based OH airglow imager likely correspond to the same event. This agreement provides independent confirmation that the concentric airglow ripples visible in the photographs correspond to the same mesospheric CGW system detected by the OH imager.

3.4 Large-scale propagation of mesospheric and lower thermospheric concentric gravity waves

During a massive red sprite cluster over the Tibetan Plateau, coordinated OH airglow imaging at Lhasa, Xining, and Xinglong shown in Fig. 7 revealed a large-scale

https://doi.org/10.5194/egusphere-2026-4160
Preprint. Discussion started: 24 July 2026

gravity wave propagating northeastward (13.4° ± 3.7° east of north) with a horizontal wavelength of 33.4 ± 4.9 km and period of 13.4 ± 2.9 min. The wave exhibited a phase speed of 42.8 ± 7.4 m s⁻¹ and spanned >16° in latitude (~30°N–46°N) and longitude, though wave amplitude and wavelength at Xinglong were notably attenuated compared to lower-latitude stations. The consistent propagation direction and wave characteristics observed across multiple stations suggest that the CGWs originated from the same deep convective system located to the south of the Himalayas. The coherent wave structures observed across multiple stations indicate persistent northeastward propagation of the concentric gravity waves over a large horizontal distance exceeding 3000 km. Such extended horizontal propagation suggests that the waves were unlikely to propagate as simple freely propagating GWs and may instead have experienced favorable propagation conditions within the MLT region.

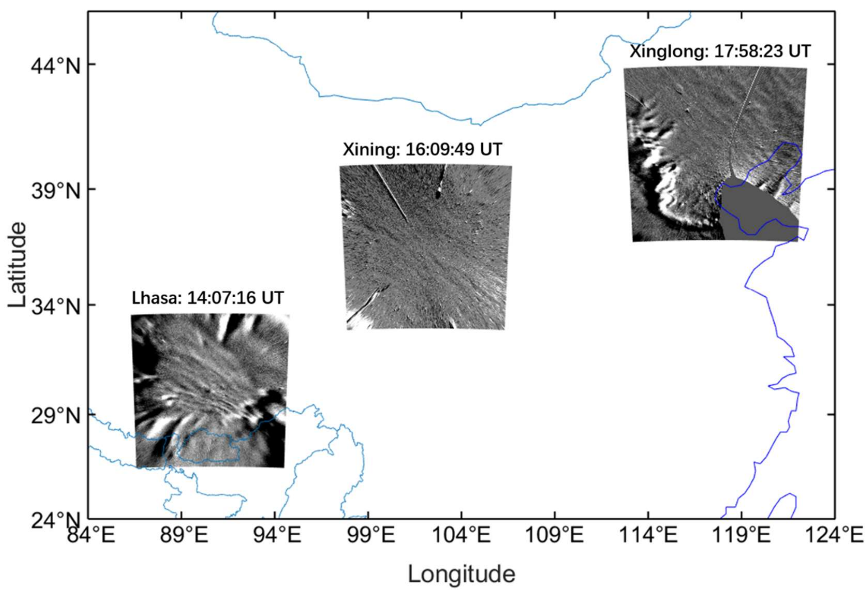

Figure 7 CGWS observed by OH airglow imagers: Lhasa station at 14:07:16 UT, Xining station at

https://doi.org/10.5194/egusphere-2026-4160
Preprint. Discussion started: 24 July 2026

16:09:49 UT, and Xinglong station at 17:58:23 UT.

To investigate the propagation characteristics of the CGWs in the MLT region, we examined the vertical wavenumber using the GW dispersion relation (Hines, 1960):

$$m^2 = \frac{N^2}{(c-u)^2} - k_H^2 - \frac{1}{4H^2} \quad , \tag{4}$$

Here, m and k_H represent the vertical and horizontal wavenumbers, respectively, derived from the airglow imaging observations; c is the observed horizontal phase speed of the gravity wave; u denotes the background wind speed in the direction of wave propagation, obtained from the SD-WACCM-X wind fields; H is the scale height; and N^2 is the Brunt–Väisälä frequency, defined as:

$$N^2 = \frac{g}{T}\left(\frac{dT}{dz} + \frac{g}{c_p}\right), \tag{5}$$

where $g = 9.54$ ms^{-2} is gravitational acceleration, T is the temperature, $c_p = 1005$ J Kg^{-1}K^{-1} is the specific heat at constant pressure, dT/dz represents the vertical temperature gradient derived from TIMED/SABER observations.

The temperature profiles used in this analysis were obtained from SABER/TIMED measurements, and the background wind conditions were characterized using SD-WACCM-X wind fields, as shown in Fig. 8. Figure 8a and b show the temperature profiles over the relevant locations on 19 May 2022, with the corresponding UTC times and locations indicated in Fig. 1. Figure 8c, d and e illustrate the wind fields for Lhasa, Xining, and Xinglong, respectively.

https://doi.org/10.5194/egusphere-2026-4160
Preprint. Discussion started: 24 July 2026

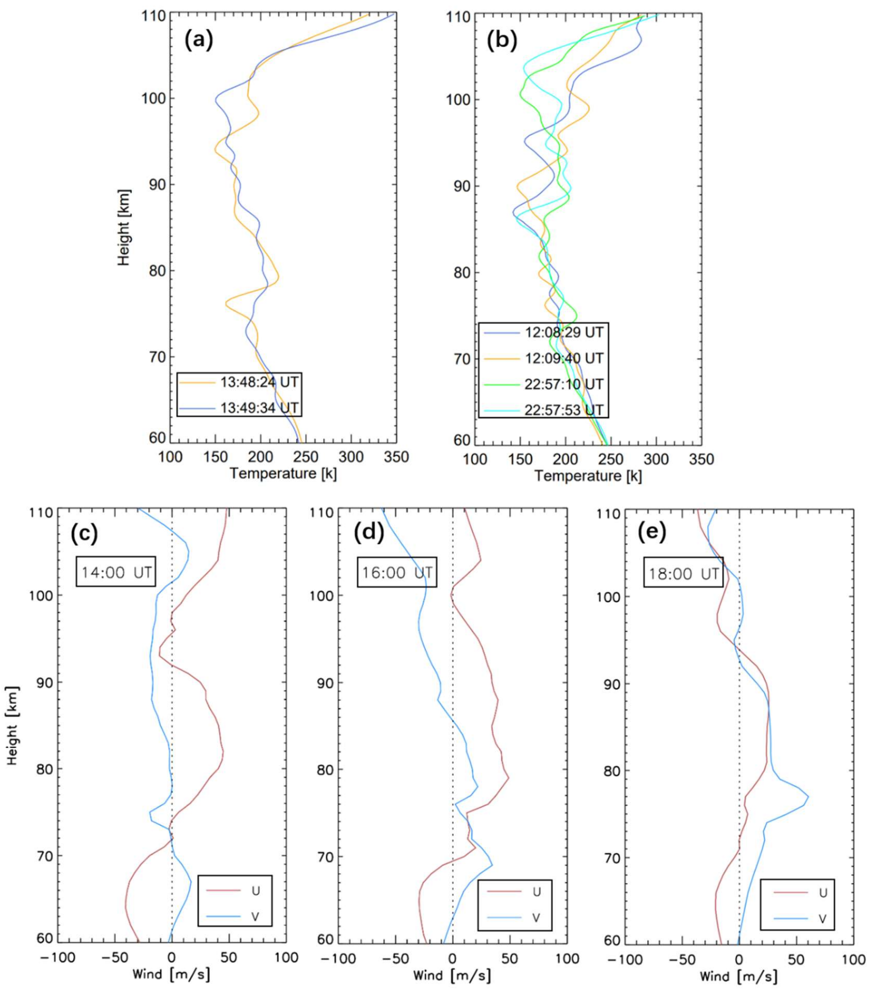

Figure 8 Temperature profiles derived from SABER/TIMED measurements (panels a and b) and SD-WACCM-X wind fields (panels c–e). (a) and (b) show profiles measured on 19 May 2022 at the following UTC times: (a) 13:48:24 and 13:49:34; (b) 12:08:29, 12:09:40, 22:57:10, and 22:57:53 (corresponding locations are marked in Fig. 1). (c), (d), and (e) present the wind fields over Lhasa, Xining, and Xinglong, respectively.

Figure 9 presents the vertical wavenumber profiles over (a) Lhasa, (b) Xining, and (c) Xinglong. The profiles reveal stable ducting layers at Lhasa (75–93 km), Xining (65–99 km), and Xinglong (70–94 km). These ducting layers suggest that the deep

https://doi.org/10.5194/egusphere-2026-4160
Preprint. Discussion started: 24 July 2026

convection-generated CGWs were able to propagate over horizontal distances exceeding 3000 km within the MLT region. The presence of positive vertical wavenumber regions bounded by evanescent layers indicates favorable waveguide conditions that can effectively trap gravity-wave energy and suppress vertical leakage. Consequently, wave energy can be transported horizontally over much greater distances than would be expected for freely propagating gravity waves. The observed propagation distance therefore highlights the critical role of MLT ducting structures in enabling large-scale horizontal transport of gravity-wave energy and momentum.

Despite the shallower duct over Lhasa, the peak OH volume emission rate there was approximately three times larger than those over Xining and Xinglong (Fig. 9). Nevertheless, comparable CGW signatures were observed at all three stations. This suggests that the visibility of the wave structures was controlled not only by the background OH emission intensity but also by the ducting characteristics and the vertical overlap between the trapped wave field and the OH emission layer. Therefore, a deeper duct may favor long-distance horizontal propagation, whereas the observed airglow perturbation amplitude is additionally influenced by local airglow conditions and wave–airglow layer coupling.

https://doi.org/10.5194/egusphere-2026-4160
Preprint. Discussion started: 24 July 2026

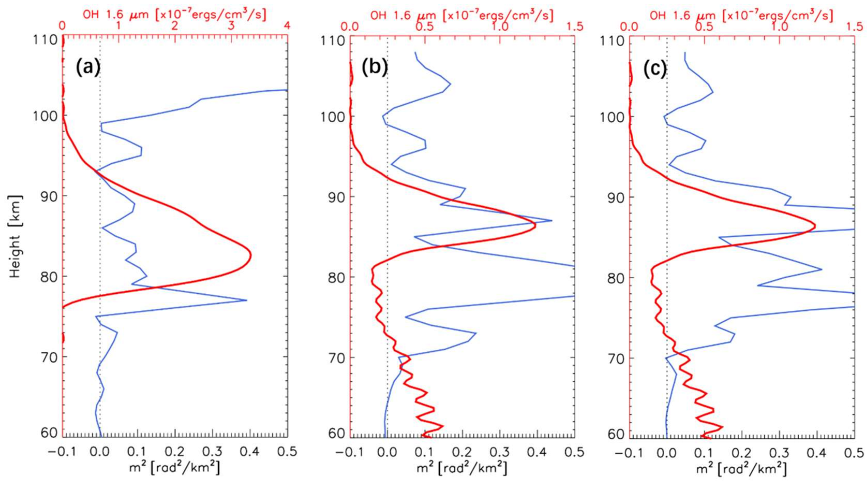

Figure 9 Vertical profiles of the vertical wave number squared (m^2) and OH 1.6 μm volume emission rates over the (a) Lhasa, (b) Xining, and (c) Xinglong stations. The profiles of m^2 are derived from temperature profiles (as shown in Fig. 8a–b) and SD-WACCM-X wind fields (as shown in Fig. 8c–e). The OH emission profiles are obtained from averaged SABER/TIMED measurements on 19 May 2022 at the following UTC times: (a) 13:48:24 and 13:49:34; (b) and (c) 12:08:29, 12:09:40, 22:57:10, and 22:57:53 (see Fig. 1 for the measurement locations).

3.5 Thermospheric concentric gravity waves by red-line (630 nm) airglow imagers

In addition to the CGWs observed in the stratosphere and MLT region, thermospheric CGWs were also identified in red-line (630.0 nm) airglow observations at the far-field Shuozhou station, as shown in Fig. 10. The observed wave fronts exhibit partial concentric arc structures propagating predominantly northeastward. The horizontal wavelength gradually increases with distance from the inferred source region, indicating characteristics consistent with wave excitation from a localized source. Fitting analysis suggests that the center of the concentric wave structures was approximately located at (31.6°N, 90.4°E).

In contrast, no comparable concentric gravity wave structures propagating toward

https://doi.org/10.5194/egusphere-2026-4160
Preprint. Discussion started: 24 July 2026

the north or northwest were detected in the red-line (630.0 nm) airglow observations at the Korla station. The distinct difference in wave occurrence between Shuozhou and Korla suggests pronounced directional asymmetry in the propagation of the thermospheric CGWs during this event.

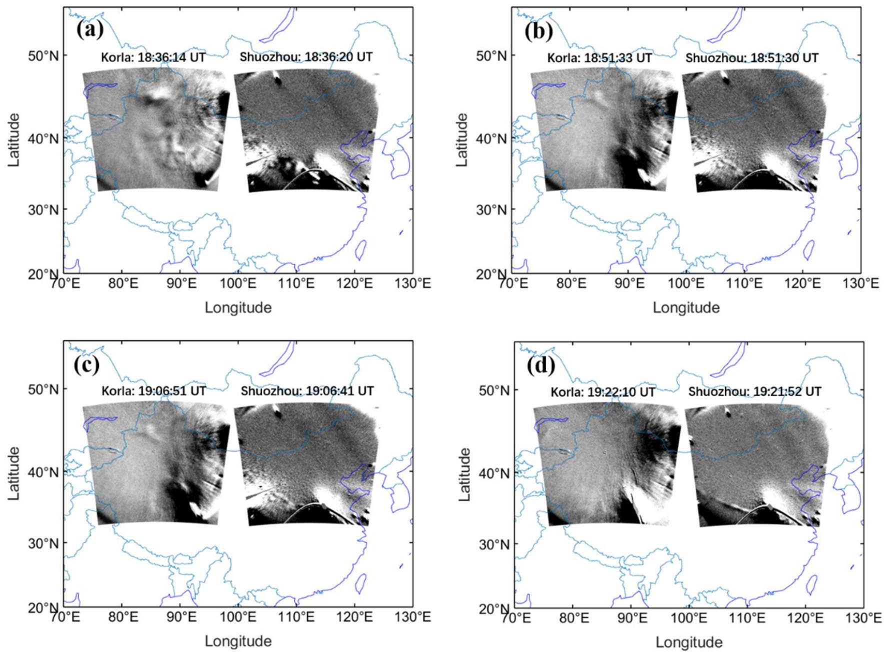

Figure 10 Red-line (630 nm) airglow observations from the Shuozhou and Korla stations. Thermospheric CGWs are clearly observed over Shuozhou, whereas no obvious CGW signatures are detected over Korla. Panels (a)–(d) correspond to 18:36, 18:51, 19:06, and 19:22 UT, respectively.

3.5.1 Potential mechanisms for the asymmetry of concentric gravity waves

Thermospheric background winds induce Doppler shifting that strongly influences the observability of AGWs through two primary mechanisms: cancellation effects within the finite airglow layer thickness and dissipative filtering. When AGWs propagate against the background wind, their intrinsic frequency increases, resulting in

https://doi.org/10.5194/egusphere-2026-4160
Preprint. Discussion started: 24 July 2026

longer vertical wavelengths. These longer vertical wavelengths reduce cancellation effects within the airglow layer and are less susceptible to dissipative processes such as molecular viscosity and thermal conduction, thereby enhancing wave detectability at thermospheric altitudes. Conversely, AGWs propagating in the same direction as the background wind experience reduced intrinsic frequencies and shorter vertical wavelengths. Such shortened vertical wavelengths enhance cancellation effects within the airglow layer and increase susceptibility to dissipative damping. As a result, these waves are more readily attenuated before reaching observable amplitudes in airglow measurements.

The westward zonal wind over the Xining region simulated by TIE-GCM (17:00-19:00 UT, 19 May 2022) shown in Fig. 11 provides a plausible explanation for the absence of CGW signatures at the Korla station. According to Doppler shift theory, westward-propagating waves traveling with the background wind would experience shortened vertical wavelengths, making them more vulnerable to both cancellation effects and dissipative filtering. In contrast, the northeastward-propagating CGWs observed at Shuozhou propagated partially against the prevailing wind, favoring longer vertical wavelengths and improved observability. These results suggest that directional filtering by thermospheric background winds likely contributed to the asymmetric distribution of the observed thermospheric CGWs.

https://doi.org/10.5194/egusphere-2026-4160
Preprint. Discussion started: 24 July 2026

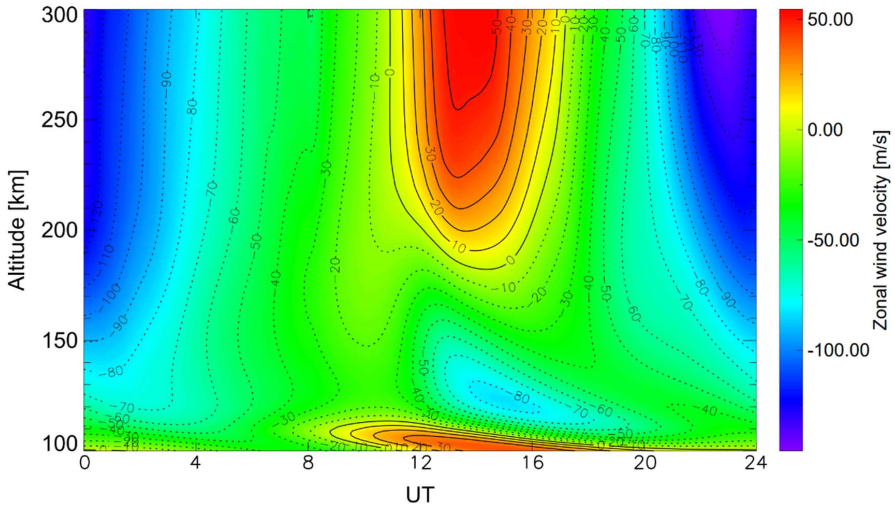

Figure 11 Zonal wind contour from the TIEGCM simulation over Xining station, from 00:00 to 24:00 UT on 19 May 2022.

3.5.2 Possible source of concentric gravity waves in the themosphere

Figure 12 illustrates the background atmospheric conditions over Shuozhou at 18:00 UT. Specifically, panel (a) shows the temperature profile and the corresponding sound speed, while panel (b) presents the background wind fields. These composite profiles are constructed using SD-WACCM-X data for the altitude range of 0–106 km and TIE-GCM data for 106–300 km. The sound speed, $c_s = \sqrt{\gamma RT}$, near the turbopause is approximately 300 m/s (see Fig. 12a), where γ is ratio of specific heats, R is specific gas constant, and T is temperature.

As demonstrated by Vadas and Crowley (2010), GWs cannot propagate vertically once their horizontal phase speed approaches or exceeds the local sound speed. This constraint arises because internal GWs depend on molecular interactions for their propagation and therefore cannot travel faster than the local sound speed. Under such conditions, the gravity wave transitions toward acoustic-wave behavior, preventing

https://doi.org/10.5194/egusphere-2026-4160
Preprint. Discussion started: 24 July 2026

vertical propagation as an internal gravity wave.

Based on this reasoning, Vadas et al. (2019) further derived the maximum allowable intrinsic phase speed for gravity wave propagation, denoted as max (c_I):

$$\max(c_I) \simeq \frac{2\sqrt{\gamma-1}}{\gamma} c_s \quad , \tag{6}$$

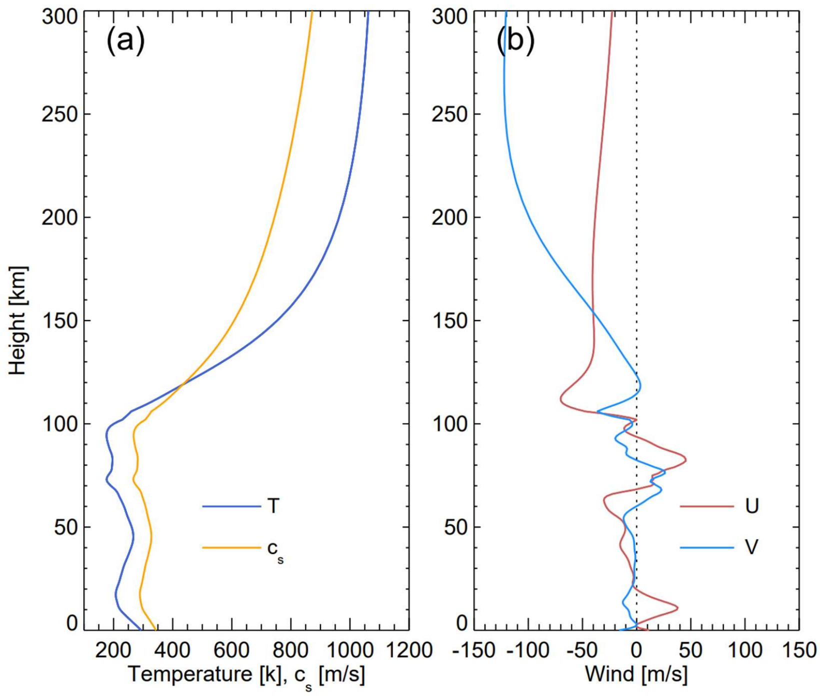

Figure 12 Background atmosphere over Shuozhou at 18:00 UT: (a) Temperature and corresponding sound speed, (b) Background atmospheric wind fields. The composite profiles are constructed using SD-WACCM-X data (0–106 km) and TIE-GCM data (106–300 km).

Based on the information from Fig. 13, which shows $c_I \Big/ \left[\frac{2\sqrt{\gamma-1}}{\gamma} c_s\right]$ as a function of horizontal phase speed c and height for CGW, a gravity wave cannot propagate when $c_I \Big/ \left[\frac{2\sqrt{\gamma-1}}{\gamma} c_s\right] \geq 1$. The thermosphere GWs observed at Shuozhou

https://doi.org/10.5194/egusphere-2026-4160
Preprint. Discussion started: 24 July 2026

station with c > 250–270 m/s must originate in the thermosphere and therefore cannot be primary GWs generated by deep convection.

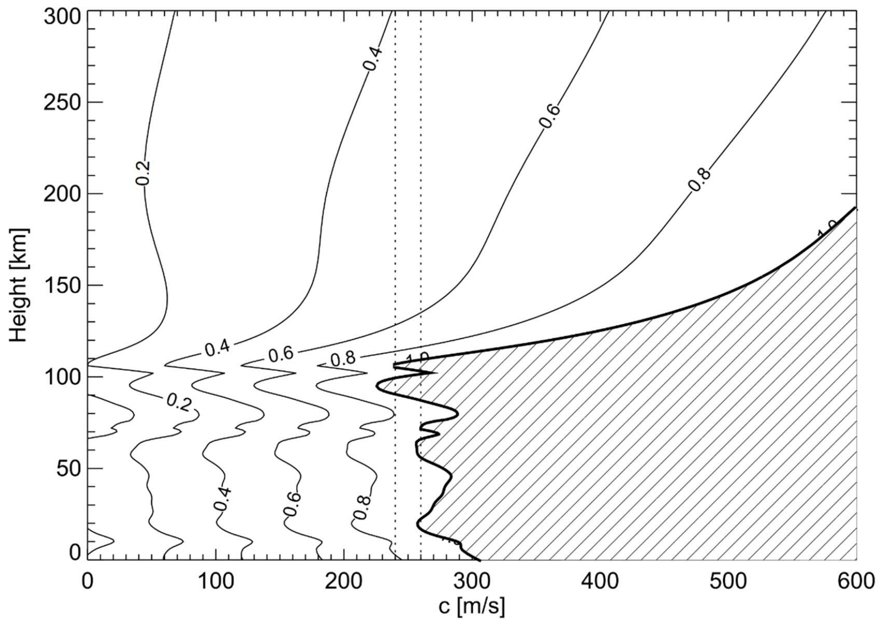

Figure 13 $c_I \Big/ \left[\frac{2\sqrt{\gamma-1}}{\gamma} c_s\right]$ as a function of c and H at 18:00 UT. The hatched regions show where $c_I \Big/ \left[\frac{2\sqrt{\gamma-1}}{\gamma} c_s\right] \geqslant 1$. The velocity range between the dashed lines represents the observed phase velocities of thermospheric CGWs.

We employed a ray-tracing method to estimate the source location of the thermospheric CGWs. The model is based on a dispersion relation that incorporates molecular viscosity and thermal diffusivity (Vadas, 2007), as given by Eq. (4). By solving this dispersion relation, we traced the propagation paths of gravity waves backward in order to identify their potential source regions in the upper atmosphere.

$$m^2 = \frac{k_H^2 N^2}{\omega_{Ir}^2 (1+\delta_+ + \delta^2/\mathrm{Pr})}\left[1+\frac{\nu^2}{4\omega_{Ir}^2}(\mathrm{k}^2-\frac{1}{4H^2})^2\frac{\left(1-\mathrm{Pr}^{-1}\right)^2}{\left(1+\delta_+/2\right)^2}\right]^{-1} - k_H^2 - \frac{1}{4H^2}, \quad (7)$$

https://doi.org/10.5194/egusphere-2026-4160
Preprint. Discussion started: 24 July 2026

where ω_{Ir} is the intrinsic frequency; $k^2 = k_H^2 + m^2$, $k_H^2 = k^2 + l^2$; H is the scale height; $\nu = \mu/\bar{\rho}$ is the kinematic viscosity where μ is the molecular viscosity and $\bar{\rho}$ is the background density; $\delta = \nu m / H\omega_{Ir}$, $\delta_+ = \delta(1 + Pr^{-1})$, where Pr is the Prandtlnumber. k, l, and m are the zonal, meridional, and vertical wave number components of the GW, respectively. The density $\bar{\rho}$ were obtained from the NRLMSISE-00 model (Picone et al., 2002).

Figure 14 shows the results of the reverse ray tracing. Figure 14a presents the latitude–longitude distribution of the rays, where p1–p7 (circles) represent the starting points of the reverse ray tracing and T1–T7 (dots) denote the corresponding ray endpoints. Figures 14b and 14c show the altitude variations of the ray trajectories as functions of latitude and longitude, respectively. Although gravity wave generation may occur anywhere along an individual ray path (Vadas and Azeem, 2021), the reverse ray trajectories exhibit clear convergence near (32.2°N, 91.7°E) at an altitude of approximately 150 km, suggesting a preferred source region for the observed thermospheric CGWs in the lower thermosphere.

Primary GWs generated by deep convection typically undergo substantial amplitude growth and dissipation as they propagate upward into the thermosphere because of the rapidly decreasing atmospheric density. As these waves approach critical levels or dissipative regimes, they can deposit momentum and energy into the background atmosphere, thereby generating secondary GWs with distinct propagation characteristics and phase speeds (Vadas et al., 2003; Vadas and Azeem, 2021). These secondary waves are capable of propagating efficiently within the thermosphere and

https://doi.org/10.5194/egusphere-2026-4160
Preprint. Discussion started: 24 July 2026

can exhibit substantially larger horizontal phase speeds than the original primary waves. The inferred source altitude near 150 km is therefore consistent with secondary wave generation associated with the dissipation and breaking of upward-propagating primary gravity waves.

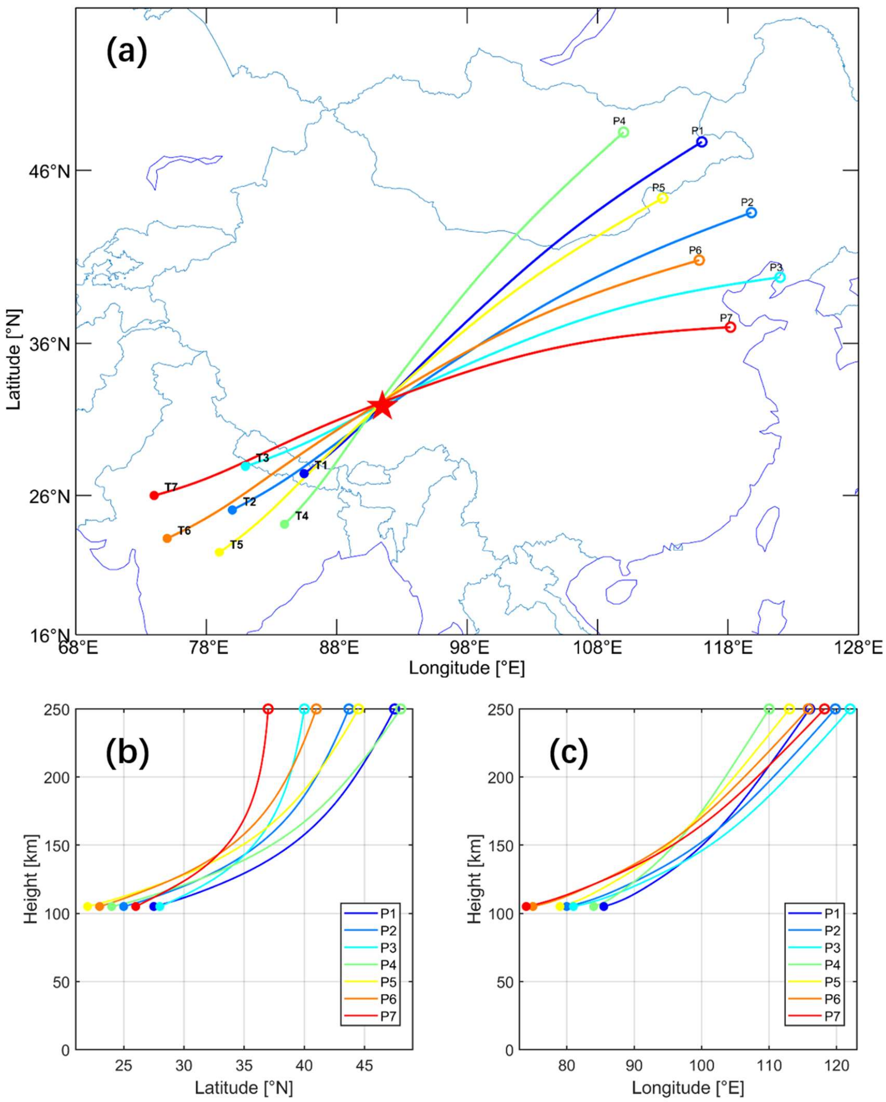

Figure 14 Reverse ray-tracing results for the thermospheric gravity wave observed at 250 km

https://doi.org/10.5194/egusphere-2026-4160
Preprint. Discussion started: 24 July 2026

altitude. (a) Horizontal propagation paths projected onto the geographic map. (b) Altitude–latitude distributions of the ray trajectories. (c) Altitude–longitude distributions of the ray trajectories. The ray paths converge toward a preferred source region near 150 km altitude.

4 Conclusions

Severe thunderstorms are important sources of energy and momentum for the middle and upper atmosphere through electrical and dynamical pathways. Electrically, intense thunderstorms generate TLEs, including red sprites, gigantic jets, and ghosts, representing strong lightning activity extending into the middle atmosphere. Dynamically, deep convection excites AGWs, which transport energy and momentum upward and can generate secondary waves through dissipation and breaking. Together, these processes provide important pathways for vertical atmospheric coupling. However, simultaneous observations of electrical and dynamical responses of extreme convective systems across multiple atmospheric layers remain rare.

To investigate the atmospheric response to this extreme convective event, we combined ground-based optical imaging, amateur photography, satellite observations, and numerical simulations. Multi-layer airglow observations characterized CGWs in the mesosphere and thermosphere through OH, OI 557.7 nm, and OI 630.0 nm emissions. Satellite observations from AIRS, TIMED/SABER, and Meteosat/SEVIRI, together with SD-WACCM-X and TIE-GCM simulations, provided information on wave activity, atmospheric conditions, and propagation environments.

The electrical response was characterized by an extraordinary TLE outbreak observed on 19 May 2022 from Lake Pumoyongcuo, southern Tibet. Time-lapse photography recorded more than 100 red sprites, 16 secondary gigantic jets, and at least

https://doi.org/10.5194/egusphere-2026-4160
Preprint. Discussion started: 24 July 2026

four ghosts between 13:00 and 16:00 UT, representing the largest documented red sprite outbreak observed from China and one of the most remarkable TLE events in the Himalayan–Bay of Bengal region. The simultaneous occurrence of multiple TLE types indicates strong electrical coupling between the storm and the middle atmosphere.

The dynamical response from the stratosphere to the mesosphere–lower thermosphere (MLT) was identified through satellite and ground-based CGW observations. AIRS and airglow imagers revealed concentric gravity-wave structures, with MLT CGWs propagating northeastward for more than 3000 km under favorable ducting conditions. These observations highlight the importance of atmospheric background conditions in sustaining long-distance gravity-wave propagation.

Thermospheric CGWs observed in the OI 630.0 nm layer exhibited horizontal phase speeds of 260–280 m s^{-1}. Reverse ray tracing suggested a source altitude near 150 km, indicating that these waves were likely secondary gravity waves generated by dissipation and breaking of primary waves. Their asymmetric distribution was likely controlled by thermospheric winds through Doppler-induced vertical wavelength changes and dissipative filtering. These results provide rare observational evidence of multi-step gravity-wave coupling from the lower atmosphere to the thermosphere during an extreme convective event.

Data availability. The multi-layer airglow network data are available from the Chinese Meridian Project Data Center at https://dcstatus.meridianproject.ac.cn (MPDC, 2026). TIMED/SABER temperature and emission intensity data are available from the

https://doi.org/10.5194/egusphere-2026-4160
Preprint. Discussion started: 24 July 2026

SABER data archive at http://saber.gats-inc.com/data.php (Russell et al., 1999). MSG/SEVIRI data are available from the EUMETView service of the European Organisation for the Exploitation of Meteorological Satellites (EUMETSAT) at https://user.eumetsat.int /data-access/eumetview (EUMETSAT, 2026). AIRS Level 1B radiance data are available from the NASA Goddard Earth Sciences Data and Information Services Center (GES DISC) at https://doi.org/10.5067/YZEXEVN4JGGJ (AIRS Project, 2007). The SD-WACCM-X and TIE-GCM 3.0 simulation outputs generated in this study are available from the corresponding author upon reasonable request.

Author contributions. QL conceived the study, conducted the data analysis, interpreted the results, and wrote the manuscript. OAV contributed to the acquisition and analysis of the SEVIRI data. AA contributed to the processing and interpretation of the red sprite imagery. XW performed the TIE-GCM 3.0 simulations and contributed to their interpretation. SG performed the SD-WACCM-X simulations and contributed to the analysis of the model results. JX, WY, and YZ contributed to the interpretation of the results and manuscript preparation. All authors discussed the results, revised the manuscript, and approved the final version.

Competing interests. The contact author has declared that none of the authors has any competing interests.

https://doi.org/10.5194/egusphere-2026-4160
Preprint. Discussion started: 24 July 2026

Acknowledgements. We acknowledge the use of data from the Chinese Meridian Project. We acknowledge the TIMED/SABER mission for providing the temperature and emission intensity data. We acknowledge the European Organisation for the Exploitation of Meteorological Satellites (EUMETSAT) for providing the Meteosat Second Generation (MSG)/SEVIRI data. We also acknowledge the NASA Goddard Earth Sciences Data and Information Services Center (GES DISC) for providing the AIRS data.

Financial support. This work was supported by the B-type Strategic Priority Program of the Chinese Academy of Sciences (CAS, Grant No. XDB0780000), the National Natural Science Foundation of China (Grant Nos. 42374205 and 41974179), and the Specialized Research Fund of National Space Science Center, Chinese Academy of Sciences (Grant No. E4PD3010). The project is also supported by the Specialized Research Fund for State Key Laboratories.

https://doi.org/10.5194/egusphere-2026-4160
Preprint. Discussion started: 24 July 2026

References

AIRS project: AIRS/Aqua L1B Infrared (IR) geolocated and calibrated radiances V005, Goddard Earth Sciences Data and Information Services Center (GES DISC) [data set], Greenbelt, MD, USA, https://doi.org/10.5067/YZEXEVN4JGGJ, 2007.

Alexander, M. J. and Holton, J. R.: On the spectrum of vertically propagating gravity waves generated by a transient heat source, Atmos. Chem. Phys., 4, 923–932, https://doi.org/10.5194/acp-4- 923-2004, 2004.

Aumann, H. H., Chahine, M. T., Gautier, C., Goldberg, M. D., Kalnay, E., McMillin, L. M., Revercomb, H., Rosenkranz, P. W., Smith, W. L., Staelin, D. H., Strow, L. L., and Susskind, J.: AIRS/AMSU/HSB on the aqua mission: Design, science objectives, data products, and processing systems, IEEE T. Geosci. Remote, 41, 253–264, https://doi.org/10.1109/TGRS.2002.808356, 2003.

Chou, C. C., Dai, J., Kuo, C. L., and Huang, T. Y.: Simultaneous observations of storm-generated sprite and gravity wave over Bangladesh, J. Geophys. Res.: Space Phys., 121(9), 9222–9233, https://doi.org/10.1002/2016JA022554, 2016.

EUMETSAT: EUMETView, available at: https://user.eumetsat.int/data-access/eumetview, last access: 20 February 2026.

Fovell, R., Durran, D., and Holton, J. R.: Numerical simulations of convectively generated stratospheric gravity waves, J. Atmos. Sci., 49, 1427–1442, https://doi.org/10.1175/1520- 0469(1992)0492.0.CO;2, 1992.

https://doi.org/10.5194/egusphere-2026-4160
Preprint. Discussion started: 24 July 2026

Fritts, D. C. and Alexander, M. J.: Gravity wave dynamics and effects in the middle atmosphere, Rev. Geophys., 41, 1003, https://doi.org/10.1029/2001RG000106, 2003.

Günzkofer, F., Liu, H., Liu, H., Stober, G., Lu, G., Wu, H., Bartel, N., Heymann, F., and Borries, C.: High-latitude joule heating in tie-gcm 3.0: Evaluation of different plasma convection forcing models, Geophysical Research Letters, 52(17), e2025GL117647, https://doi.org/10.1029/2025GL117647, 2025.

Heale, C. J., Snively, J. B., Bhatt, A. N., Hoffmann, L., Stephan, C. C., and Kendall, E. A.: Multilayer observations and modeling of thunderstorm-generated gravity waves over the Midwestern United States, Geophys. Res. Lett., 46, 14164–14174, https://doi.org/10.1029/2019GL085934, 2019.

Heale, C. J., Inchin, P. A., and Snively, J. B.: Primary Versus Secondary Gravity Wave Responses at F-Region Heights Generated by a Convective Source, J. Geophys. Res.-Space, 127,e2021JA029947, https://doi.org/10.1029/2021JA029947, 2022.

Hines, C. O.: Internal atmospheric gravity waves at ionospheric heights, Can. J. Phys., 38, 1441–1481, https://doi.org/10.1139/p60-150, 1960.

Hoffmann, L. and Alexander, M. J.: Occurrence frequency of convective gravity waves during the North American thunderstorm season, J. Geophys. Res., 115, D20111, https://doi.org/10.1029/2010JD014401, 2010.

Hoffmann, L., Alexander, M. J., Clerbaux, C., Grimsdell, A. W., Meyer, C. I., Rößler, T., and Tournier, B.: Intercomparison of stratospheric gravity wave observations

https://doi.org/10.5194/egusphere-2026-4160
Preprint. Discussion started: 24 July 2026

with AIRS and IASI, Atmos. Meas. Tech., 7, 4517–4537, https://doi.org/10.5194/amt-7- 4517-2014, 2014.

Holton, J. R.: The influence of gravity wave breaking on the general circulation of the middle atmosphere, J. Atmos. Sci., 40, 2497–2507, https://doi.org/10.1175/1520-0469(1983)0402.0.CO;2, 1983.

Huang, H. L., Lu, G. P., An, A., Xu, D., Cheng, Z. W., Wang, Y. P., Chen, Y. Z., and Huang, X.: Massive outbreak of red sprites in South Asia observed from the Tibetan Plateau, Adv. Atmos. Sci., 42, 1247–1260, https://doi.org/10.1007/s00376-024-4143-5, 2025.

Hurrell, J. W., Holland, M. M., Gent, P. R., Ghan, S., Kay, J. E., Kushner, P. J., Lamarque, J.-F., Large, W. G., Lawrence, D., Lindsay, K., Lipscomb, W. H., Long, M. C., Mahowald, N., Marsh, D. R., Neale, R. B., Rasch, P., Vavrus, S., Vertenstein, M., Bader, D., Collins, W. D., Hack, J. J., Kiehl, J., & Marshall, S.: The Community Earth System Model: A framework for collaborative research, Bulletin of the American Meteorological Society, 94, 1339–1360. https://doi.org/10.1175/BAMS-D-12-00121.1, 2013.

Lai, C., Li, P. W., Xu, J. Y., Yuan, W., Yue, J., Liu, X., Masaru, K., and Qian, L. L.: Joint observation of the concentric gravity wave event on the Tibetan Plateau, Earth Planet. Phys., 6(3), 219–227, https://doi.org/10.26464/epp2022029, 2022.

Li, Q., Xu, J., Liu, H., Liu, X., and Yuan, W.: How do gravity waves triggered by a typhoon propagate from the troposphere to the upper atmosphere?, Atmos. Chem.

https://doi.org/10.5194/egusphere-2026-4160
Preprint. Discussion started: 24 July 2026

Phys., 22, 12077–12091, https://doi.org/10.5194/acp-22-12077-2022, 2022.

Li, Q., Xu, J., Gusman, A. R., Liu, H., Yuan, W., Liu, W., Zhu, Y., and Liu, X.: Upper-atmosphere responses to the 2022 Hunga Tonga–Hunga Ha'apai volcanic eruption via acoustic gravity waves and air–sea interaction, Atmos. Chem. Phys., 24, 8343–8361, https://doi.org/10.5194/acp-24-8343-2024, 2024.

Li, Q., Xu, J., Zhu, Y., Wrasse, C. M., Bageston, J. V., Yuan, W., Liu, X., Liu, W., Wen, Y., Li, H., and Liu, Z.: Extreme concentric gravity waves observed in the mesosphere and thermosphere regions over southern Brazil associated with fast-moving severe thunderstorms, Atmos. Chem. Phys., 25, 9719–9736, https://doi.org/10.5194/acp-25-9719-2025, 2025.

Liu, H.-L., Bardeen, C. G., Foster, B. T., Lauritzen, P., Liu, J., Lu, G., . . . Wang, W.: Development and validation of the Whole Atmosphere Community Climate Model with thermosphere and ionosphere extension (WACCM-X 2.0). Journal of Advances in Modeling Earth Systems, 10, 381–402. https://doi.org/10.1002/2017MS001232, 2018.

Maurya, A. K., Parihar, N., Dube, A., Singh, R., Kumar, S., Olivier, C., et al.: Rare observations of sprites and gravity waves supporting D, E, F-regions ionospheric coupling, Scientific Reports, 12(1), 581, https://doi.org/10.1038/s41598-021-03808-5, 2022.

MPDC: Airglow data [data set], https://dcstatus.meridianproject.ac.cn/#/sjfw/sjjs, last access: 12 January 2026.

https://doi.org/10.5194/egusphere-2026-4160
Preprint. Discussion started: 24 July 2026

Nyassor, P. K., Wrasse, C. M., Paulino, I., São Sabbas, E. F. M. T., Bageston, J. V., Naccarato, K. P., Gobbi, D., Figueiredo, C. A. O. B., Ayorinde, T. T., Takahashi, H., and Barros, D.: Sources of concentric gravity waves generated by a moving mesoscale convective system in southern Brazil, Atmos. Chem. Phys., 22, 15153–15177, https://doi.org/10.5194/acp-22-15153-2022, 2022.

Pasko, V. P., Inan, U. S., and Bell, T. F.: Sprites as evidence of vertical gravity wave structures above mesoscale thunderstorms, Geophys. Res. Lett., 24(14), 1735–1738, https://doi.org/10.1029/97GL01607, 1997.

Passas-Varo, M., van der Velde, O., Gordillo-Vázquez, F. J., et al.: Spectroscopy of a mesospheric ghost reveals iron emissions, Nat. Commun., 14, 7810, https://doi.org/10.1038/s41467-023-42892-1, 2023.

Peng, C.-H., and Chen, X.: Monsoonal MCS initiation, rainfall, and diurnal gravity waves over the Bay of Bengal: Observation and a linear model, Atmos. Chem. Phys., 24, 1401–1418, https://doi.org/10.5194/acp-24-1401-2024, 2024.

Picone, J. M., Hedin, A. E., Drob, D. P., and Aikin, A. C.: NRLMSISE-00 empirical model of the atmosphere: Statistical comparisons and scientific issues, J. Geophys. Res., 107, 1468, https://doi.org/10.1029/2002JA009430, 2002.

Plane, J. M. C., Gumbel, J., Kalogerakis, K. S., Marsh, D. R., and von Savigny, C.: Opinion: Recent developments and future directions in studying the mesosphere and lower thermosphere, Atmos. Chem. Phys., 23, 13255–13282, https://doi.org/10.5194/acp-23-13255-2023, 2023.

https://doi.org/10.5194/egusphere-2026-4160
Preprint. Discussion started: 24 July 2026

Richmond, A. D., Ridley, E. C., and Roble, R. G.: A thermosphere/ionosphere general circulation model with coupled electrodynamics, Geophysical Research Letters, 19(6), 601–604, https://doi.org/10.1029/92GL00401, 1992.

Russell III, J. M., Mlynczak, M. G., Gordley, L. L., Tansock, J., and Esplin, R.: An overview of the SABER experiment and preliminary calibration results, Proc. SPIE, 3756, 277–288, https://doi.org/10.1117/12.366382, 1999.

Schmetz, J., Pili, P., Tjemkes, S., Just, D., Kerkmann, J., Rota, S., and Ratier, A.: An introduction to Meteosat Second Generation (MSG), Bulletin of the American Meteorological Society, 83, 977–992, https://doi.org/10.1175/1520-0477(2002)083<0977:AITMSG>2.3.CO;2, 2022.

Sentman, D., Wescott, E., Picard, R., Winick, J., Stenbaek-Nielsen, H., Dewan, E., and Morrill, J.: Simultaneous observations of mesospheric gravity waves and sprites generated by a midwestern thunderstorm, J. Atmos. Sol.-Terr. Phys., 65, 537–550, https://doi.org/10.1016/S1364-6826(02)00328-0, 2003.

Smith, S. M., Vadas, S. L., Baggaley, W. J., Hernandez, G., and Baumgardner, J.: Gravity wave coupling between the mesosphere and thermosphere over New Zealand, J. Geophys. Res.- Space, 118, 2694–2707, https://doi.org/10.1002/jgra.50263, 2013.

Smith, S. M., Setvák, M., Beletsky, Y., Baumgardner, J., and Mendillo, M.: Mesospheric gravity wave momentum flux associated with a large thunderstorm complex, J. Geophys. Res.-Atmos., 125, e2020JD033381,

https://doi.org/10.5194/egusphere-2026-4160
Preprint. Discussion started: 24 July 2026

https://doi.org/10.1029/2020JD033381, 2020.

Vadas, S. L., Fritts, D. C., and Alexander, M. J.: Mechanism for the generation of secondary waves in wave breaking regions, J. Atmos. Sci., 60, 194–214, https://doi.org/10.1175/1520- 0469(2003)0602.0.CO;2, 2003.

Vadas, S. L.: Horizontal and vertical propagation and dissipation of gravity waves in the thermosphere from lower atmospheric and thermospheric sources, J. Geophys. Res.-Space, 112, A06305, https://doi.org/10.1029/2006JA011845, 2007.

Vadas, S. L., and Crowley, G.: Sources of the traveling ionospheric disturbances observed by the ionospheric TIDDBIT sounder near Wallops Island on October 30, 2007, Journal of Geophysical Research: Space Physics, 115, A07324, https://doi.org/10.1029/2009JA015053, 2010.

Vadas, S. L., and Azeem, I.: Concentric secondary gravity waves in the thermosphere and ionosphere over the continental United States on March 25–26, 2015 from deep Convection. Journal of Geophysical Research: Space Physics, 126, e2020JA028275. https:// doi.org/10.1029/2020JA028275, 2021.

Vadas, S. L., Xu, S., Yue, J., Bossert, K., Becker, E., and Baumgarten, G.: Characteristics of the quiet-time hotspot gravity waves observed by GOCE over the Southern Andes on 5 July 2010, Journal of Geophysical Research: Space Physics, 124, 7034–7061, https://doi. org/10.1029/2019JA026693, 2019.

van der Velde, O. A., Montanyà, J., López, J. A., et al.: Gigantic jet discharges evolve stepwise through the middle atmosphere, Nat. Commun., 10,

https://doi.org/10.5194/egusphere-2026-4160
Preprint. Discussion started: 24 July 2026

4350, https://doi.org/10.1038/s41467-019-12261-y, 2019.

Wang, Y. P., Lu, G. P., Ma, M., Zhang, H. B., Fan, Y. F., Liu, G. J., Wan, Z. R., Wang, Y., Peng, K. M., Peng, C. Z., Liu, F. F., Zhu, B. Y., Ni, B. B., Gu, X. D., Chen, L., Yi, J., and Zhou, R. X.: Triangulation of red sprites observed above a mesoscale convective system in North China, Earth Planet. Phys., 3(2), 111–125, https://doi.org/10.26464/epp2019015, 2019.

Yue, J., and Lyons, W. A.: Structured elves: Modulation by convectively generated gravity waves, Geophys. Res. Lett., 42, 1004–1011, https://doi.org/10.1002/2014GL062612, 2015.